

CO₂ infrared spectra on silicate dust grain analogs: Implications for JWST observations

TUSHAR SUHASARIA,¹ VANESSA LEUSCHNER,^{1,2} CORNELIA JÄGER,^{1,3} CAROLINE GIESER,¹ AND THOMAS HENNING¹

¹*Max Planck Institute für Astronomie, Königstuhl 17, 69117, Heidelberg, Germany*

²*Department for Physics and Astronomy, University of Heidelberg, Im Neuenheimer Feld 226, 69120, Heidelberg, Germany*

³*Laboratory Astrophysics Group at the Friedrich Schiller University Jena,
Institute of Solid State Physics, Helmholtzweg 3, 07743, Jena, Germany*

ABSTRACT

Carbon dioxide is one of the three most abundant species within the ice mantles around dust grains inside molecular clouds. Since a substantial amount of interstellar grains is made of siliceous materials, we have studied the infrared profile of CO₂ deposited on top of a bare and ice-coated amorphous silicate (MgFeSiO₄) film using reflection absorption infrared spectroscopy (RAIRS). In contrast to a metal surface, the CO₂ IR profile shows a relaxation of the metal surface selection rule in the presence of the bare MgFeSiO₄ dust grain analog, which brings the IR profile closer to the observational spectra while maintaining the sensitivity of RAIRS. Experiments with the underlying CO and CH₄ ices show that their presence facilitates structural changes toward crystalline ice for the deposited CO₂ at much lower temperatures than on the polar ice layers. Warming-up experiments of CO₂ showed that it tends to stay on the silicate surface for much longer than on the gold surface without the silicate layer. We noticed for the first time a split in the ¹³CO₂ IR feature on the pure or ice-covered silicate grain as a marker for the onset of diffusion. The laboratory ¹³CO₂ profile then closely resembles recent JWST observations of this feature around young and embedded protostars, suggesting that it can be linked to the observed feature.

1. INTRODUCTION

In cold, dense regions of molecular clouds, before star formation begins, molecules like H₂O, NH₃, and CH₄ form on submicron-sized interstellar dust grains through grain surface chemistry. These molecules accumulate as ice layers, creating the first polar phase, which also contains CO₂. CO, formed in the gas phase, subsequently accretes on top of the polar phase, forming the apolar phase (Boogert et al. 2015). Additional molecules such as CH₃OH and CO₂ also form in this apolar phase, which means that CO₂ can be present in both phases (Pontoppidan et al. 2008). H₂O is the main ice component and, although it is mostly amorphous at low temperatures, it can undergo a structural transition to a cubic crystalline form as molecular clouds evolve (Jenniskens & Blake 1994).

CO₂ ice, with an abundance of 10-20% relative to H₂O in dense regions of low-mass star-forming clouds, as revealed in the mid-infrared by recent JWST obser-

ations (McClure et al. 2023), is a major carbon-bearing species. Together with CO, it contributes significantly to the overall carbon budget, providing a vital source of elemental carbon for the formation of complex organic molecules. CO₂ is a linear molecule with four fundamental vibrational modes. While the symmetric stretching mode ν_1 , is inactive in the IR, the bending mode ν_2 , which involves symmetric in-plane and out-of-plane bending, is active in the IR around 660 cm⁻¹ (Ehrenfreund et al. 1996; Pontoppidan et al. 2008; Suhasaria et al. 2017), as is the asymmetric stretching mode ν_3 near 2350 cm⁻¹ (Ehrenfreund et al. 1996; Gerakines et al. 1999). Furthermore, two combination bands ($\nu_1 + \nu_3$) around 3708 cm⁻¹ and ($2\nu_2 + \nu_3$) near 3600 cm⁻¹ (Gerakines et al. 1999) are also observed in the mid-infrared. The ¹³CO₂ isotope shows a small absorption peak around 2280 cm⁻¹ (Ehrenfreund et al. 1997).

In addition to vibrational modes, CO₂ optical phonon modes due to lattice vibrations can also appear in mid-infrared spectra under certain conditions. In the laboratory with transmittance infrared spectroscopy at normal incidence, only transverse optical (TO) phonons are excited, seen as the typical ν_2 and ν_3 modes. However, when transmittance infrared spectroscopy is performed

at oblique incidence (Baratta et al. 2000; Cooke et al. 2016), or in reflection absorption infrared spectroscopy (RAIRS) with light polarized parallel to the plane of incidence, both the ν_2 and ν_3 modes split, generating additional longitudinal optical (LO) modes. This phenomenon occurs only when the film thickness on the surface is smaller than the wavelength of the incident radiation (Berreman 1963).

For this reason, astronomical infrared spectra are usually compared with laboratory transmission spectra obtained at normal incidence. However, interstellar alignment arising from asymmetric dust grains could produce polarized radiation in star forming regions, potentially generating optical phonon modes (Andersson et al. 2015). In such scenarios, comparisons with RAIRS or oblique-incidence transmittance spectra become necessary. Although, this comparison could still be challenging due to the presence of these additional phonon modes. Nevertheless, RAIRS is preferred to transmission infrared spectroscopy for studying physical changes in thin film of ice layers due to its higher sensitivity.

Although many previous laboratory studies have examined binary mixtures of CO₂ ice with common interstellar ice components (e.g. Ehrenfreund et al. 1997, 1999; Cooke et al. 2016) there are fewer studies on CO₂ layers sequentially deposited above or below these components (van Broekhuizen et al. 2006; Edridge et al. 2013). These studies have been invaluable for interpreting interstellar ice observations, but the influence of the underlying grain surface on the infrared profile remains unexplored. The study of layered CO₂ ices is also important because CO₂ prefers to cluster with itself and segregate from ice mixtures rather than remain mixed with other components when heated above 50 K (Öberg et al. 2009), effectively forming a layered structure.

In this work, we explore three key effects on the CO₂ infrared profile: (1) the influence of an amorphous MgFeSiO₄ dust grain analog layer, (2) the impact of polar and apolar ice layers on top of the silicate surface, and (3) the changes observed during the warming of both ice layered systems until CO₂ desorption. The infrared data were then qualitatively compared with observational data from the James Webb Space Telescope obtained along the lines of sight of young and embedded protostars, particularly in relation to the ¹³CO₂ profile.

2. EXPERIMENTAL

2.1. Setup

The setup consists of an ultra-high vacuum (UHV) chamber and two triply differentially pumped and highly collimated molecular beam lines, which has been described in detail in prior works (He et al. 2016; He &

Vidali 2018). Here we briefly summarize the main features of the setup that are most relevant for the present study. The UHV chamber is a 10 inch diameter stainless steel chamber which is pumped by a combination of scroll pumps, turbomolecular pumps, and a cryopump to a base pressure of 2×10^{-10} mbar after bake-out.

A bare polished gold-plated copper disk and a thin film of amorphous MgFeSiO₄ grains deposited on its surface were used as samples. The dust film on the disk was prepared by pulsed laser ablation of a rotating Mg-Fe silicate target in a quenching gas atmosphere of He/O₂ with a ratio of 6:1 at 6 Torr pressure. The exact method including the extraction and condensation of the grains onto the disk is described in detail in Sabri et al. (2013). The prepared samples were characterized by high-resolution transmission electron microscopy to determine the composition and internal structure as well as particle sizes, and by field-emission electron microscopy to determine the general morphology. Individual amorphous silicate grains with diameters between 4 and 8 nm forming chain-like aggregates were confirmed. The porosity of the films was found to be close to 90%, leading to a surface-area-to-mass ratio of ~ 1000 m² g⁻¹. A quartz crystal microbalance was used to monitor the thickness of ~ 100 nm of film on the gold plated-copper disk.

The substrate has been changed between different sets of experiments. First, the gold plated copper disk was clamped to the cold finger of the closed-cycle helium cryostat, followed by the silicate grain coated disk. The samples can be cooled down to 10 K and locally heated up to 300 K using a 50 W resistive heater situated right behind the sample holder. The temperature was measured using a calibrated silicon diode sensor and controlled by a Lakeshore 336 temperature controller to an accuracy of 0.05 K. A thermal radiation shield surrounds the sample and insulates it by reducing the radiative heat transfer from the surrounding. Carbon monoxide (CO) (99.97 per cent; Westfalen AG), methane (CH₄) (99.995 per cent; Westfalen AG), carbon dioxide (CO₂) (99.995 per cent; Westfalen AG), water (H₂O) and methanol (CH₃OH) (Emparta ACS) were deposited on the samples from the background through two UHV variable leak valves (VAT variable leak valve 590), one of which was reserved for liquids and the other for gasses. Although the gas was used without further purification, the liquids underwent three freeze-pump-thaw cycles to remove dissolved air. The CH₃OH:H₂O (1:1) mixture was prepared in a separate mixing glass bulb by adjusting the vapor pressure ratio of the purified liquids. The mixing ratio was verified by measuring the quadrupole mass spectrometer signal

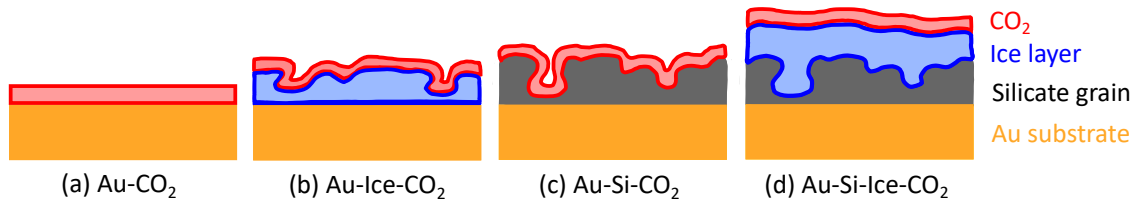


Figure 1. Schematic of the layered systems: CO₂ deposited on (a) bare gold (Au), (b) water ice on gold, (c) a silicate film on gold, and (d) ice on a silicate film on top of gold. In panel (b), the ice layers consist of different thicknesses of pASW, while in panel (d), the ice layers are either apolar (CO, CH₄) or polar (pASW, CW, CH₃OH, or CH₃OH:H₂O in a 1:1 ratio).

during deposition. The molecules were deposited on the samples at 15 K. The chamber is equipped with a Fourier transform infrared (FTIR) spectrometer (Bruker Invenio R) and a MCT detector for the analysis. Infrared spectra were collected after ice deposition and also during warming-up experiments with a linear ramp rate of 1 K min⁻¹ across a temperature range of 15 to 160 K. These measurements were taken in the RAIRS configuration, with a grazing incidence angle of 78°, covering the spectral range from 5000 to 800 cm⁻¹ with a resolution of 1 cm⁻¹. After deposition, 128 scans were recorded, while during warming-up scans were taken at every 5 K.

2.2. Methods

2.2.1. Procedure

We conducted three sets of experiments. The differently layered systems that were used are visualized in Figure 1. In the first set, we examined the effect that (c) a thin amorphous silicate layer deposited on a gold surface has on the RAIRS spectra of pure CO₂. The results were compared to measurements performed on (a) a bare gold. Furthermore, we investigated the impact of (b) varying water ice thicknesses on the RAIRS spectra of CO₂ compared to both the gold and silicate surfaces.

In the second set, we studied how the infrared profile of CO₂ changes when present on top of (d) pure and mixed polar and apolar ice layers. For pure ices, we selected common species such as H₂O, CO, CH₄, and CH₃OH, while a CH₃OH:H₂O (1:1) was used as the surface for the mixed ice. In all cases, pure or mixed ice layers were deposited first, followed by CO₂ ice. At 15 K, the water ice layer exhibited an amorphous structure and was highly porous, hence denoted porous amorphous solid water (pASW). We also performed experiments on crystalline water (CW) by depositing water at 150 K, holding it at that temperature, and then cooling it back to 15 K. We used two different coverages of CO₂ in the ice layers for comparison.

In the final set of experiments, we conducted warming experiments on the ice layers visualized in panel (d) of Figure 1 using the higher CO₂ coverages from the second set to ensure a high signal-to-noise ratio across all peaks. These measurements were intended to determine the temperatures at which CO₂ molecules undergo orientational changes, crystallization, and diffusion, as well as the onset of desorption.

2.2.2. Coverage determination

The molecular column density (molecules cm⁻²) of the deposited ices is calculated from a modified Beer–Lambert Equation (1) to account for the RAIRS mode configuration (Ioppolo et al. 2022).

$$C = \ln(10) \frac{\sin(\theta)}{2A} \int \tau(\nu) d\nu \quad (1)$$

where $A(\nu)$ is the band strength (in cm molecule⁻¹), $\tau(\nu)$ is the optical depth and $\theta = 12^\circ$ is the angle of incidence of the IR light with respect to the substrate. The column density was then expressed in terms of a monolayer (ML, around 10¹⁵ molecules cm⁻²). The band strengths are taken from Bouilloud et al. (2015), with Table 1 summarizing the values and integration ranges used.

3. RESULTS AND ANALYSIS

3.1. Effect of silicate grain on CO₂ IR profiles

We deposited ~1 ML of CO₂ on the gold surface at 15 K as seen in Figure 2 (a). We observed only the LO mode at 2363 cm⁻¹, indicative of a disordered amorphous state. According to the metal surface selection rule (MSSR), only the perpendicular components of molecular vibrations are infrared active and can be observed using RAIRS (Fulker et al. 2025). This explains why, on a bare gold surface, only the LO component was detected. We also observed a broad red shoulder. Furthermore, we detected weak and broad signals for two combination bands: ($\nu_1 + \nu_3$) at 3706 cm⁻¹ and ($2\nu_2 + \nu_3$) at 3600 cm⁻¹, along with a ¹³CO₂ peak at

species	band	integration range [cm ⁻¹]	band strength [cm molecule ⁻¹]
CO ₂	asymmetric ¹² CO ₂ stretch ν_3	2379-2332	$6.8 \cdot 10^{-17}$
CO	¹² CO stretch ν_1	2160-2127	$1.12 \cdot 10^{-17}$
CH ₄	C-H stretch ν_3	3029-2990	$1.1 \cdot 10^{-17}$
H ₂ O	O-H stretch ν_3	3672-3060	$1.5 \cdot 10^{-16}$
CH ₃ OH	C-O stretch ν_8	1065-1018	$1.07 \cdot 10^{-17}$

Table 1. The values for the band strength are taken from Bouilloud et al. (2015).

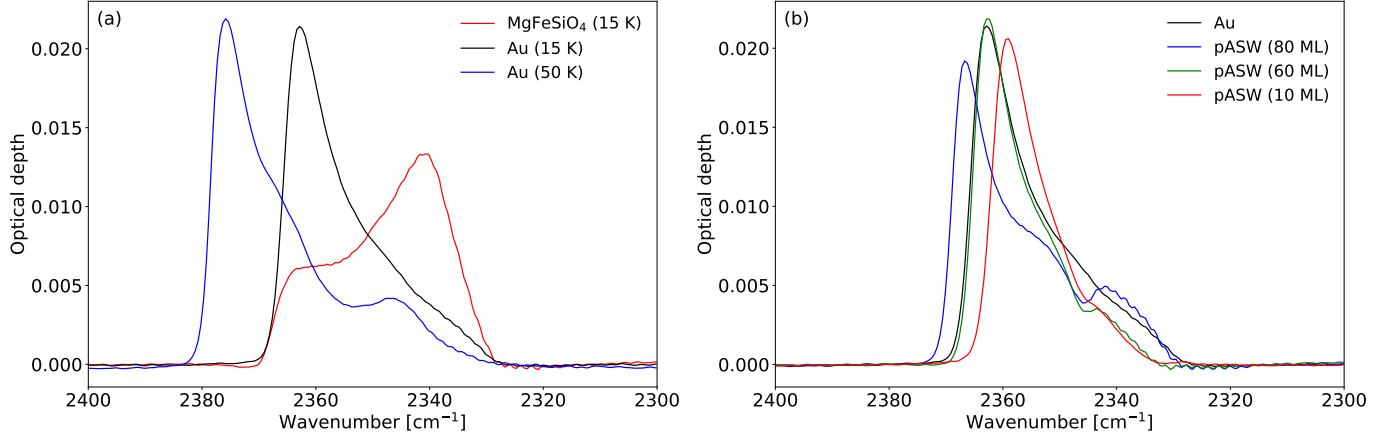


Figure 2. (a) RAIRS spectra of ~ 1 ML CO₂ (ν_3 vibrational mode) deposited on bare gold at 15 and 50 K and on gold coated with a 100 nm amorphous silicate film at 15 K. (b) Spectra of ~ 1 ML CO₂ deposited on varying thickness of porous amorphous water layers on gold at 15 K are shown alongside the spectrum on bare gold for comparison.

2280 cm⁻¹ (not shown in Figure 2). When CO₂ was deposited on the gold surface at 50 K, the LO mode blue shifted to 2376 cm⁻¹ and a small TO mode appeared at 2346 cm⁻¹. In addition to the TO mode, a weak shoulder appeared at 2365 cm⁻¹ that replaced the broad red shoulder observed at 10 K. The two combination modes became sharper, but their band positions remained nearly the same, while the ¹³CO₂ peak blue shifted to 2283 cm⁻¹, probably due to the fact that CO₂ ice is already crystalline. The appearance of a small TO mode for CO₂ deposited at 50 K on a bare gold surface was not surprising, as it has already been seen when 30 ML CO₂ ice deposited on gold at 10 K was heated to around 60 K (He & Vidalı 2018). This indicates that MSSR could be influenced by the ice phase.

In another experiment, when a similar amount of CO₂ was deposited on a silicate-covered gold surface at 15 K, the LO mode at 2363 cm⁻¹ was significantly reduced, while the TO mode was enhanced and appeared at 2341 cm⁻¹. This suggests that the MSSR was relaxed on the grain film, despite the presence of the underlying metal layer. A similar behavior was previously noted when N₂O films were deposited on copper covered with amorphous silica, with a more pronounced effect for a silica film thickness of around 300 nm (Lasne et al. 2015). In our case, the effect was observed with a silicate film of

only 100 nm thickness. The comparison is relevant because the stretching mode band strength of N₂O (Fulvio et al. 2009) is very similar to that of CO₂. However, it is also possible that the grain composition, in addition to thickness, influences MSSR. The combination modes and ¹³CO₂ feature remained unaffected by the presence of silicates. At 50 K, the TO mode remained unchanged and the LO mode is blue shifted to 2376 cm⁻¹, similar to the behavior observed on gold. Other modes followed the same pattern as CO₂ deposited on gold at 50 K, hence they are not shown.

3.2. Impact of amorphous water layer with varying thickness on CO₂ IR profiles on a bare gold surface

To check whether this relaxation of MSSR could be achieved without the silicate layer, water ice of three different thicknesses was deposited directly on gold. We then compared the infrared behavior of ~ 1 ML CO₂ on these water ice layers to the same CO₂ thickness on gold, as shown in Figure 2 (b). With a 10 ML thick water ice layer, the CO₂ infrared spectrum closely resembled that on bare gold, except that the LO peak was red-shifted to 2359 cm⁻¹. When 60 ML of water ice was deposited, the behavior remained similar to gold, especially with regard to the peak position, but a small TO peak appeared at 2343 cm⁻¹. At 80 ML thickness, the TO peak became

stronger, and the LO peak blue-shifted to 2367 cm⁻¹; however, unlike with silicates, the MSSR was not fully relaxed. This emphasizes the continued influence of the underlying grain surface on the infrared behavior.

RAIRS measurements rely on the reflective properties of metal surfaces, which do not accurately represent the composition of cosmic dust grains mainly made of carbonaceous and siliceous materials that are primarily amorphous (Henning 2010). Additionally, the absorption profiles of the CO₂ stretching mode are influenced by both the polarization and the incidence angle of the radiation. As a result, direct comparisons between observational data and laboratory measurements in RAIRS are challenging. Our results indicate that the enhancement of the LO mode is reduced when the metal surface is coated with a layer of amorphous silicate material, making RAIRS spectra more comparable to transmission spectra that only show peaks at the position of the typical TO mode. Based on this, we propose that laboratory RAIRS studies on grain coated or grain and ice layers on metal surfaces provide more reliable references for observational data, keeping the advantage of RAIRS intact, as these spectra have a higher sensitivity at the sub-monolayer/monolayer coverage regime. This approach enables RAIRS spectra to be used for qualitative comparisons, making the technique more versatile.

3.3. Effect of polar/apolar ices on top of the silicates on CO₂ IR profiles

Figure 3 shows the RAIRS spectra of CO₂ deposited on apolar ices (CO, CH₄), polar ices (pASW, CW, and CH₃OH), a polar ice mixture (CH₃OH:H₂O), and directly on silicate grains (MgFeSiO₄) without an additional ice layer. To investigate the effect on the ¹³CO₂ peak and the combination modes, additional RAIRS spectra were also recorded for 7 ML of CO₂ deposited on silicate grains, with and without an additional ice layer. When an additional layer of ice was deposited on silicates, the TO mode still appeared stronger than the LO mode for the case where 1 ML of CO₂ was added. However, for a higher CO₂ coverage, the LO mode increases in intensity and becomes nearly equal in intensity to the TO mode. Depending on the additional layer, we see differences in the band positions for both LO and TO modes of CO₂, clearly showing the effect of the chemical environment.

A clearer separation between the LO and TO vibrational modes and a deeper trough is observed when 1 ML CO₂ is deposited on apolar ices, compared to polar ices as evident in Figure 3 (a) and (b). For CO₂ on CH₄, CW, or directly on silicates, the TO mode appears closer to 2340 cm⁻¹, whereas in all other cases it appears near

2345 cm⁻¹. The LO mode is blue-shifted to 2367 cm⁻¹ for CO₂ on CH₄ and to 2363 cm⁻¹ on silicates, while for the remaining cases, it appears close to 2360 cm⁻¹. The CO₂ peaks on CO appear slightly sharper than on other ice layers which becomes clear when a higher coverage (7 ML) of CO₂ is added.

In the case of 7 ML CO₂ deposited on a CH₄ layer, the TO mode appears at nearly the same position as on silicate, while the LO mode is slightly blue-shifted to 2376 cm⁻¹ as evident in Figure 3 (c). In contrast, for CO₂ deposited on a CO layer, both the LO and TO modes are blue-shifted to 2378 and 2345 cm⁻¹, respectively, with the LO mode appearing sharper compared to those on silicate or CH₄-covered silicate. This sharpening and blue shift can be attributed to the CO₂ being deposited on pre-existing polycrystalline CO ice (He et al. 2021). The ¹³CO₂ feature at 2280 cm⁻¹ and the combination modes at 3705 and 3598 cm⁻¹ remain similar for CH₄ on silicate and bare silicate. However, for CO on silicate, all features are sharper and blue-shifted to 2283, 3709, and 3600 cm⁻¹, respectively.

When CO₂ is deposited onto these polar ices or mixtures, the peak shapes and positions are not significantly affected as seen in Figure 3 (d). CO₂ deposited on silicate and crystalline water (CW) displays notable similarity with minimal separation between the LO and TO modes, despite the underlying layer being fully crystalline in the case of CW. In contrast to CO₂ on polycrystalline CO, the crystalline nature of CW does not sharpen the CO₂ features. The LO mode is blue-shifted by 1 cm⁻¹ for CW compared to silicate.

For CO₂ deposited on other polar ices or ice mixtures, the LO and TO modes are more clearly separated than on silicate. The TO mode appears at 2345, 2346, and 2343 cm⁻¹, while the LO mode is found at 2375, 2375, and 2376 cm⁻¹ for pASW, CH₃OH, and CH₃OH:H₂O, respectively. There is no noticeable shift in the ¹³CO₂ peak or the combination modes.

3.4. Effect of heating on CO₂ IR profile

As CO₂ ice is heated from 15 K, it starts to undergo a phase transition, rearranging from a disordered amorphous state to a micro-/polycrystalline structure. With further heating, the ice crystallizes fully at a specific temperature. As the temperature continues to rise, the CO₂ molecules begin to diffuse across the surface, and at sufficiently high temperatures, they desorb, which means that they leave the surface (see Escribano et al. (2013) for an extensive discussion on the temperature effects on the CO₂ IR profile). How these four physical phenomena are affected by CO₂ present on a bare gold surface, a silicate-covered gold surface and 10 ML

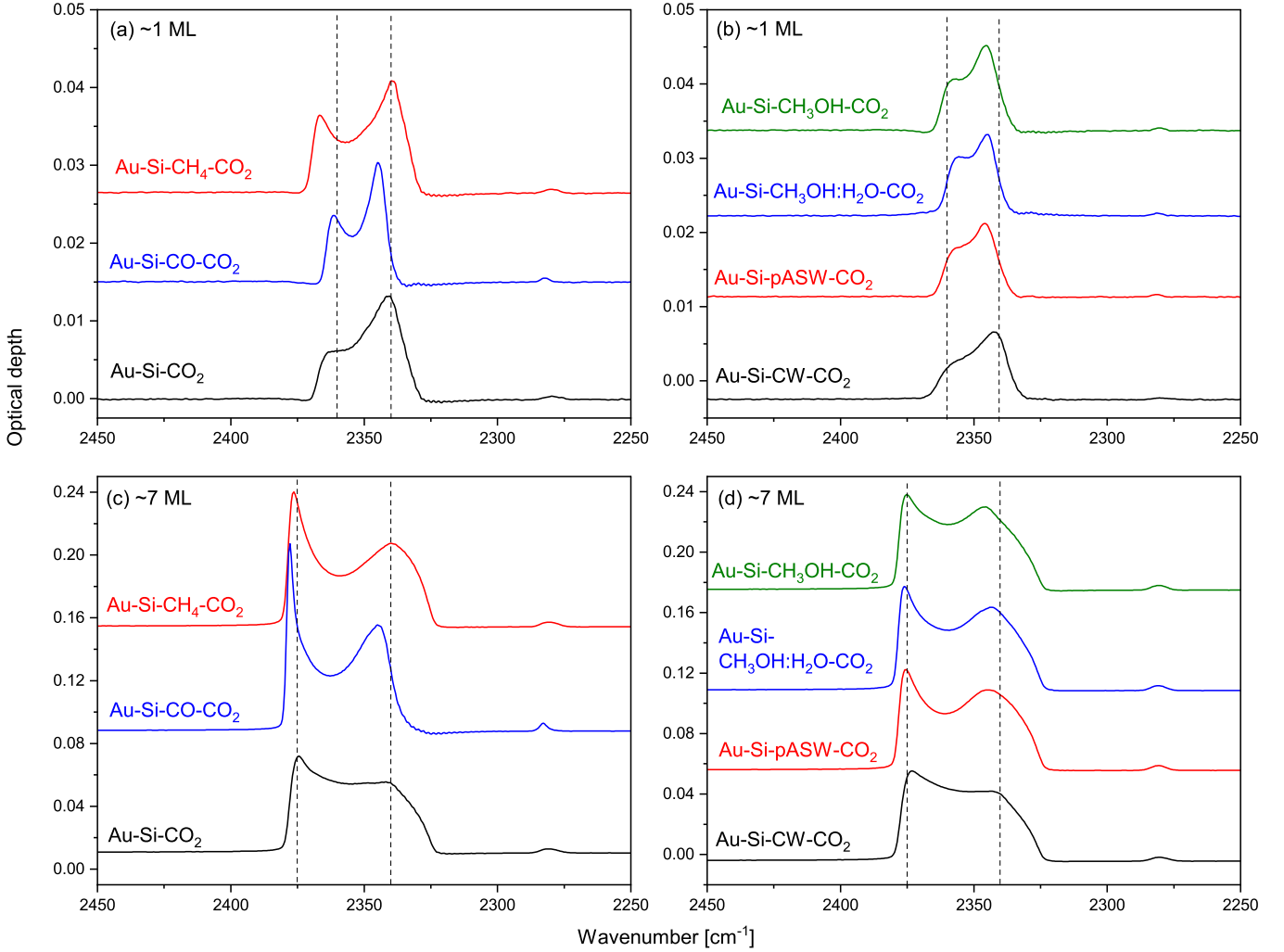


Figure 3. RAIRS spectra of CO_2 (ν_3 vibrational mode) deposited at 15 K on gold coated with a 100 nm amorphous silicate film, with or without an additional ~ 10 ML layer of pure or mixed ice. The top column shows 1 ML CO_2 spectra on (a) the silicate film without additional ice layer and on pure apolar ices, (b) on pure polar ices and an ice mixture. The bottom panels (c) and (d)

display the corresponding spectra for 7 ML of CO_2 . Spectra have been vertically offset for clarity. Vertical lines at 2375, 2360 and 2340 cm^{-1} , provides a visual reference. The first two values (2375 and 2360 cm^{-1}) are typically close to the LO mode, while the latter value (2340 cm^{-1}) to the TO mode.

additional ice layer on a silicate covered gold surface is shown in Figure 4.

3.4.1. Phase transition

During the phase transition, the ν_3 bands for $^{12}\text{CO}_2$, $^{13}\text{CO}_2$, and the combination modes ($\nu_1 + \nu_3$) and ($2\nu_2 + \nu_3$) sharpen. The LO and TO modes blue shift to higher wavenumbers, ~ 2379 cm^{-1} and ~ 2345 cm^{-1} , respectively, for all the cases. The ν_3 band for $^{13}\text{CO}_2$ and the combination modes also blue shift by ~ 2 cm^{-1} . For the ν_3 band of $^{12}\text{CO}_2$, the combined effect of blue shift and the peak sharpening begins at 35 K for all cases, except for CO, CH_4 , and CW. As mentioned earlier, CO ice is already polycrystalline at 15 K, so CO_2 de-

posited on CO ice is already in a more ordered state, and no changes occur from 15 K to above 40 K. For CH_4 , the transition occurs between 25 and 30 K, since the underlying CH_4 surface also undergoes reorientation within this range (Emtiaz et al. 2022). Although CW is fully crystalline, CO_2 ice deposited at 15 K does not initially orient toward a more ordered state, with the phase transition occurring later, around 45 K. A possible explanation is that on a surface with a mixed phase (partially amorphous and crystalline), nucleation for crystalline ice phase growth is already present. In contrast, on fully crystalline CW water, there is a lack of pre-existing nucleation sites.

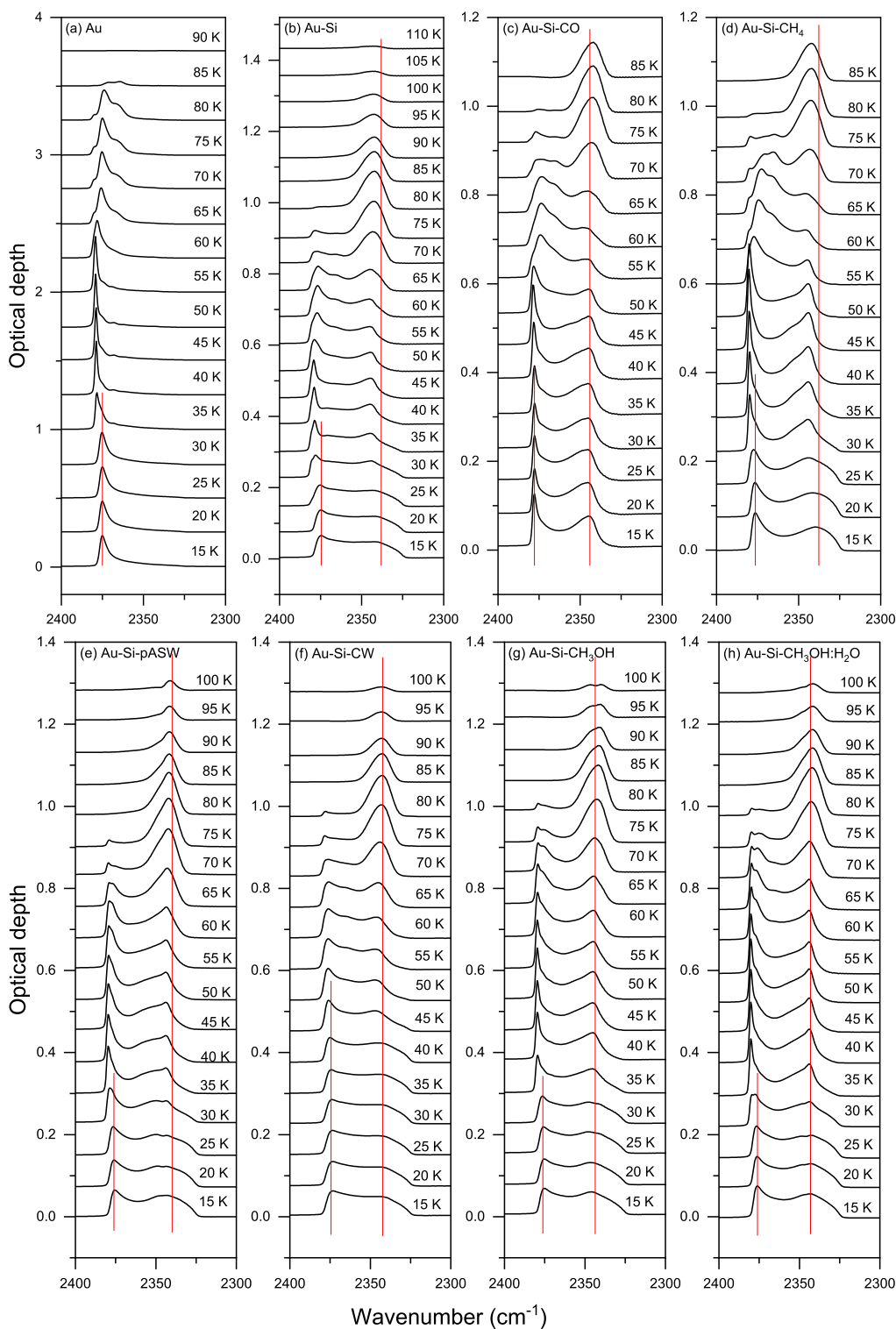


Figure 4. RAIRS spectra of ~ 7 ML CO₂ (ν_3 vibrational mode) during heating from 15 K to 160 K. The CO₂ was deposited on bare gold, gold coated with a 100 nm amorphous silicate film, and on silicate films with an additional layer of pure or mixed ice (~ 10 ML). The temperatures at each stage of heating are labeled above each curve, with spectra for silicate/silicate-ice layers offset by 0.075 and those on gold offset by 0.25 for clarity. The top row displays CO₂ spectra on: (a) bare gold, (b) the silicate film, (c) CO on silicate film, and (d) CH₄ on silicate film. The bottom row presents spectra for ice layers on silicate films: (e) porous amorphous solid water (pASW), (f) crystalline water (CW), (g) pure CH₃OH, and (h) CH₃OH:H₂O mixture. The vertical lines at close to LO and TO position provides a visual reference.

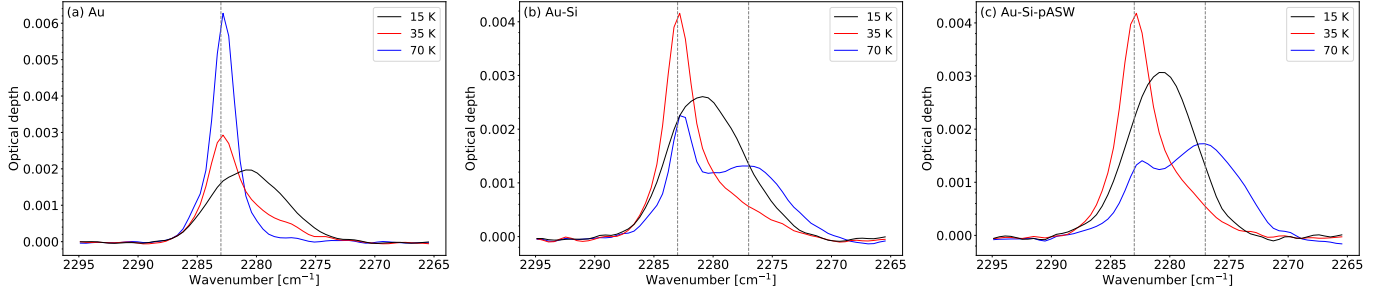


Figure 5. RAIRS spectra of ~ 7 ML CO_2 (ν_3 $^{13}\text{CO}_2$ vibrational mode) shown at selected temperatures during warming up. The CO_2 was deposited on (a) bare gold, (b) gold coated with a 100 nm amorphous silicate film, and on (c) a silicate film with 10 ML pASW ice on top. The vertical lines at 2283 and 2277 cm^{-1} provide a visual reference.

3.4.2. Complete crystallization

As the CO_2 ices on different surface layers are heated beyond 35 K, all the bands become sharper and so no significant shifts occur. The combination mode serves as a more reliable complete crystallinity marker, as it exhibits the same behavior in both reflection and transmission modes (He & Vidali 2018). When this mode is at its sharpest, it indicates nearly complete crystallization. In all cases, the sharpest combination mode occurs almost around 50 K, aligning well with the temperature range reported in previous studies (Falk & Seto 1986; Isokoski et al. 2013).

3.4.3. Diffusion

For CO_2 deposited on top of the bare and ice-covered silicate grain, a new peak at 2276 cm^{-1} appears at 60 K as a red shoulder to the ν_3 band of $^{13}\text{CO}_2$. As the temperature increases, it grows in intensity. By 75 K, it develops into a double peak as seen in panels (b) and (c) of Figure 5. The growth of the double peak feature cannot be observed for CO_2 deposited on gold without the silicate and is hence not visible in panel (a). Previous studies show that CO_2 diffusion on non-porous ASW becomes active above 60 K (He et al. 2024), allowing molecules to either form island clusters on the surface or penetrate through the bulk of water ice surface, both of which can affect the infrared peak profiles. A clearer effect on the ν_3 band of $^{12}\text{CO}_2$ may require investigation with sub-monolayer coverages (He et al. 2017). Previous studies with pure CO_2 showed no significant changes around 60 K for the ν_3 band of $^{13}\text{CO}_2$ (He & Vidali 2018), but the underlying silicate layer in this experiment influenced the outcome. The initial red-shoulder peak serves as a marker for the onset of diffusion. On the other hand, the combination modes remain largely unaffected.

3.4.4. Additional features during the warming up process

For the ν_3 band of $^{12}\text{CO}_2$, three additional changes in the IR peak profile were observed during warming

up. First, LO mode intensity variations occur between 65 and 70 K, where the LO mode intensity decreases and subsequently the TO mode intensity increases. On gold, which only exhibits the LO mode, no decrease is observed until desorption begins. Second, starting at 60 K, the sharp LO mode undergoes a red shift for CO_2 on gold as well as on the CO and CH_4 ices, the latter two exhibiting larger shifts, probably due to their desorption. No shifts are observed for CO_2 on CW, CH_3OH , or $\text{CH}_3\text{OH}:\text{H}_2\text{O}$, while a small blue shift appears at 70 K in the case of the bare silicate substrate, although its cause remains unclear. Third, shoulder peaks emerge between the LO and TO mode at different temperatures and band positions depending on the surface. On gold, they appear at 40 K at 2375 and 2368 cm^{-1} and shift to 2380 and 2366 cm^{-1} at 65 K. On silicates, they arise at 35 K at 2371 cm^{-1} and shift to 2365 cm^{-1} at 55 K. For CO, the shoulder emerges at 60 K at 2365 cm^{-1} , while for CH_4 , it appears at 30 K at 2376 cm^{-1} and persists until 50 K, with new shoulders at 2380 and 2371 cm^{-1} forming at 60 K. On pASW, the shoulder remains between 65 and 75 K at 2376 cm^{-1} , while on CW, it is present between 55 and 65 K at 2364 cm^{-1} . For CH_3OH , shoulders emerge at 2376 and 2371 cm^{-1} at 35 K and persist until 80 K, whereas for $\text{CH}_3\text{OH}:\text{H}_2\text{O}$, they appear at 2376 cm^{-1} at 50 K and remain until 80 K. In all cases, the shoulder peaks persist until the LO mode intensity declines.

Edridge et al. (2013) observed a shoulder peak at 2373 cm^{-1} for CO_2 adsorbed on graphite at 28 K, attributing it to a heterogeneous and amorphous CO_2 layer that disrupts phonon vibrations and modifies IR interactions. Upon heating to 55 K, this peak shifted to 2367 cm^{-1} . Additionally, a feature at 2361 cm^{-1} was detected in a 15% $\text{CH}_3\text{OH}:\text{H}_2\text{O}$ ice mixture at 30 K, likely due to interactions between CO_2 and CH_3OH (Edridge et al. 2013). Similarly, a peak at 2365 cm^{-1} was identified when a CO_2 and H_2O mixture was deposited between 50 and 80 K, attributed to CO_2 trapped within partially ordered amorphous H_2O ice (Sandford & Allaman-

dola 1990). Furthermore, DFT calculations have shown that vibrational bands from clusters of up to five CO₂ molecules in water can contribute to a peak at 2367 cm⁻¹ (Tychengulova et al. 2024). The present study confirms the complexity of these shoulder peaks, which arise from dipole-dipole interactions between CO₂ and surrounding species, spanning from amorphous to crystalline forms. Importantly, this shoulder peak should not be mistaken for the X mode, which is described by [Escribano et al. \(2013\)](#) as a low frequency shoulder to the ν_3 band of ¹²CO₂ at 2328 cm⁻¹.

3.4.5. Desorption

Starting at 85 K, the infrared features of CO₂ on gold show a significant decrease in intensity, and beyond 90 K, the IR signal of CO₂ disappears completely. This marks the desorption temperature of CO₂ on the gold surface. In contrast, for CO₂ on silicate-coated gold, only the TO mode is observed at 85 K. Desorption begins beyond this temperature and completes between 115 and 120 K, which is significantly higher than on the gold surface. The porous nature and the likely presence of various binding sites on the silicate film cause CO₂ to remain bound to the surface much longer than on gold. The desorption temperatures for ice layers on silicate films were not determined, as all surfaces, except for the CW surface, undergo changes during the warming process. The volatile species CO and CH₄ are expected to desorb before CO₂, while pASW, CH₃OH, and CH₃OH:H₂O could trap some CO₂ in their pores and release it at higher temperatures. The desorption of these species from the same silicate grain has been studied using temperature programmed desorption experiments, the results of which will be published in an upcoming manuscript. Based on this study it can be said that most of CO and CH₄ desorbs around 70 K.

4. ASTROPHYSICAL IMPLICATIONS

There are two important implications of our work. First, we observed a significant increase in the desorption temperature of CO₂ on our dust grain analogue, an amorphous silicate surface, compared to gold. About 50% of CO₂ remained adsorbed on the silicate surface until a temperature of 88 K, while at that temperature CO₂ on the gold surface was nearly fully desorbed. This suggests that CO₂ will return to the gas phase much later during the warm-up phase of star formation in silicate grain environments. Consequently, more CO₂ molecules will remain locked in the solid state, increasing the likelihood of their active participation in grain surface chemistry for the formation of complex organic molecules. The higher binding energy of CO₂ on silicate grains will also shift the CO₂ snowline in protoplanetary

disks to higher temperatures, which could influence the planet formation process ([Minissale et al. 2022](#)).

Second, our laboratory infrared spectra of ¹³CO₂ on silicates and silicates covered by additional ice layers pure or in mixtures revealed a distinct double peak profile at 70 K that was absent on the gold surface. In particular, this double peak structure resembles recent JWST observations of ¹³CO₂ toward the young, embedded protostars HOPS 370 and IRAS 20216 ([Brunken et al. 2024](#)). The observed ¹³CO₂ spectral profiles were analyzed in the past by fitting them with combinations of laboratory ¹³CO₂ spectra obtained at different temperatures and for different ice mixtures. The best fit was achieved using a combination of three different profiles, which are warm CO₂:CH₃OH at 105 K, hot CO₂:H₂O at 160 K, and pure CO₂ at 80 K (see Figure 5 in [Brunken et al. \(2024\)](#)). However, none of the individual profiles exhibited a double-peak profile.

For completeness, previous laboratory measurements of ¹³CO₂ infrared spectra have shown a distinct double-peaked profile in transmission only above 110 K, when CO₂ was mixed with H₂O and CH₃OH. In these cases, the double peak was attributed to the segregation of CO₂ from the ice mixture ([Boogert et al. 2000](#)). These laboratory ¹³CO₂ profiles were then used also for interpretation of ISO-SWS observations along 13 galactic lines of sight, including high- and low-mass protostars and molecular clouds ([Boogert et al. 2000](#)).

To compare our laboratory spectra with observations, we use archival JWST data obtained with the Near-Infrared Spectrograph (NIRSpec) from the Investigating Protostellar Accretion (IPA) program ([Federman et al. 2024; Brunken et al. 2024](#)). Following the analysis by [Brunken et al. \(2024\)](#), we extract the NIRSpec spectrum, F_{obs} , from the source positions (listed in Table A.1 in [Brunken et al. 2024](#)) with an aperture radius of 0.6". We estimate the local continuum, F_{cont} , by fitting a cubic polynomial considering both sides of the ¹³CO₂ absorption feature at 4.4 μm ($\approx 2280 \text{ cm}^{-1}$). The optical depth spectrum is then calculated as $\tau_\nu = -\ln(F_{\text{obs}}/F_{\text{cont}})$. The optical depth spectra of low and high luminous sources are presented in Fig. 6. The dip beyond 2270 cm⁻¹ is due to emission of the H₂ S(10) transition.

Our comparison shows that CO₂ ice deposited on both bare and ice-covered silicates at temperatures around 70 K (on laboratory timescales) can qualitatively match not only the double-peaked infrared spectral profile of ¹³CO₂ observed with JWST on high luminous sources as seen in Figure 6 (b) but also the shoulders on the low luminous sources in Figure 6 (a), regardless of whether the underlying ice layers are apolar (CO, CH₄) or polar

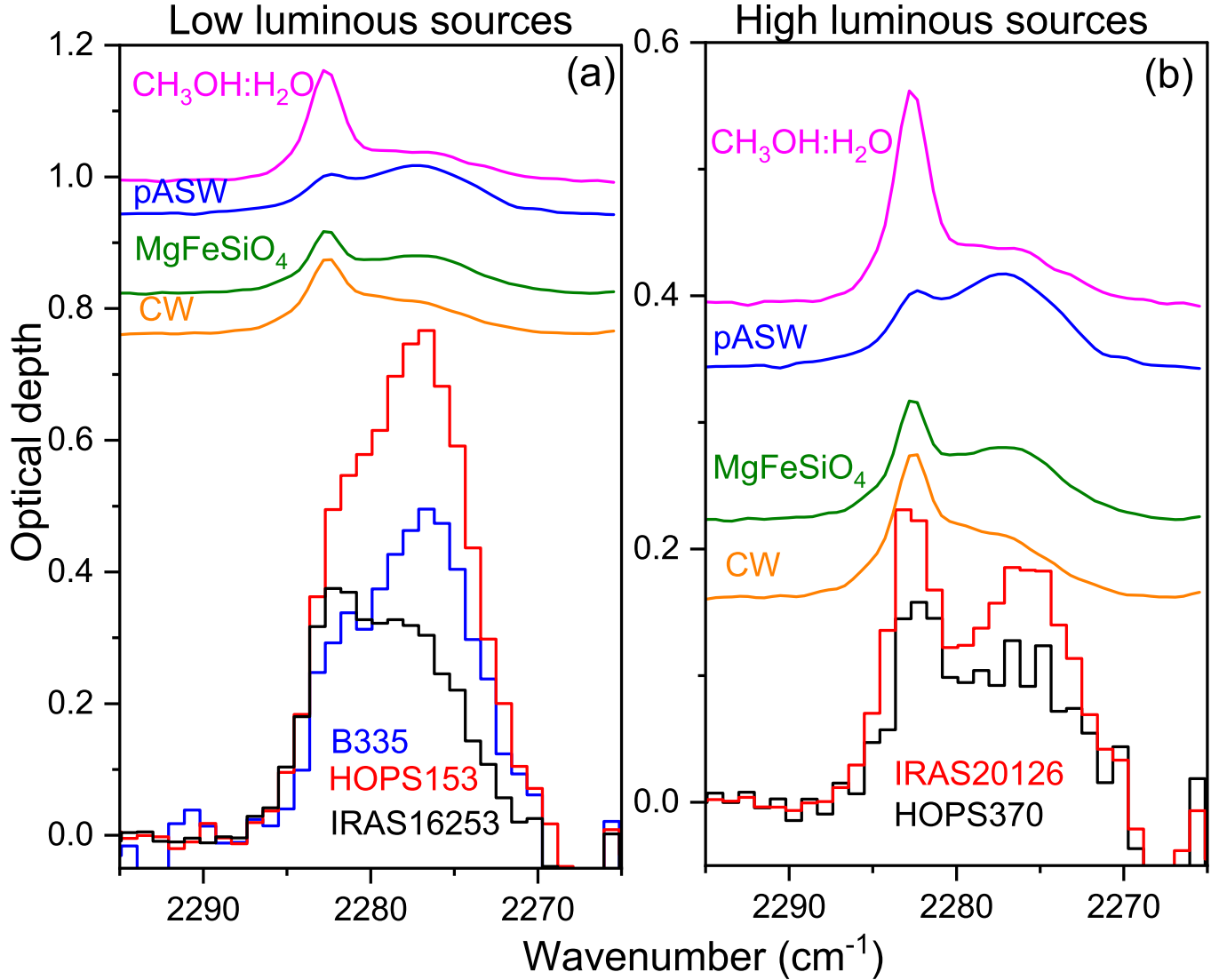


Figure 6. Comparison of the $^{13}\text{CO}_2$ ice feature toward (a) low luminous and (b) high luminous protostars with laboratory spectra on different surfaces. To facilitate comparison, all laboratory spectra have been scaled by a factor of 40. Additionally, in panel (b), the $\text{CH}_3\text{OH}:\text{H}_2\text{O}$ spectrum is vertically offset by 0.4, while in panel (a), all laboratory spectra from panel (b) are offset by 0.6.

(pASW, CW, CH_3OH and $\text{CH}_3\text{OH}:\text{H}_2\text{O}$). The advantage that our experiments have is that each individual component exhibits a distinct double-peaked profile, so the effect can be attributed solely to the grain surface and there is no need to invoke only CO_2 mixed in polar ices at high temperatures. Despite the high luminosity of the sources, it is unlikely that the entire environment will reach uniformly elevated temperatures. Furthermore, we also calculated the full width half maximum (FWHM) of HOPS 370 and IRAS 20126 to be ~ 12.5 and ~ 13 cm^{-1} , respectively. In comparison, the $^{13}\text{CO}_2$ profile on both silicate and pASW on silicate at 70 K shown in Figure 5 has a FWHM of ~ 10.5 cm^{-1} . The broadness of the observational spectra therefore indicate that

multiple laboratory components are needed for a better spectral match. For the other young embedded protostars observed by Brunken et al. (2024) that were not as luminous as HOPS 370 and IRAS 20126, our laboratory profiles of CO_2 ices in polar and apolar layers deposited on silicates at temperatures at or below 70 K can be used to nicely fit the profile as well as the shoulders of the observed peaks.

5. CONCLUSION

We observed a significant effect of the underlying amorphous silicate dust grain analog on the CO_2 RAIRS profile. When a silicate film was applied to a gold-coated copper disk, it suppressed the LO mode, which typically dominates on gold due to the MSSR, and enhanced the

TO mode, which is typically seen in transmission spectra. To isolate the impact of the silicate grain, we also conducted experiments with bare gold surfaces covered by pASW with varying ice thicknesses representing typical ISM coverages. The CO₂ spectra on pASW closely matched those on the bare gold surface. Our results suggest that the relaxation of the MSSR occurs only when the metal surface is covered by a thin film of dust grain analog. This approach maintains the high sensitivity of RAIRS while providing spectra more comparable to observational data, an effect not achievable with ice layers alone, as far as water-experiments are concerned.

In the layered ice experiments, where CO₂ was deposited on CO, we found that structural orientation toward crystalline ice occurred as early as the deposition temperature of 15 K. When CO₂ was deposited on CH₄, structural changes in CO₂ occurred between 25 and 30 K. During subsequent warming experiments, we observed that even when CO₂ was deposited on pre-existing crystalline water ice layers, the structural orientation occurred at higher temperatures compared to amorphous polar and apolar ice layers. Furthermore, compared to an gold surface, silicate dust grains were found to extend the CO₂ desorption temperature, which would result in CO₂ remaining in the solid state for a longer period on the astrophysical timescales, allowing more time for chemical reactions to occur to form more complex organic molecules.

In the warming experiments, we also examined the effect of heating on different CO₂ RAIRS modes. Notably, for the ¹³CO₂ stretching mode, we observed a splitting

of the feature around 70 K which did not occur on gold. This split feature closely matched recent JWST observations of young and embedded protostars, which show a similarly split isotopologue feature. In the past, the profile was attributed to contributions from CO₂ in different ice mixtures at different temperatures. Based on our study, we propose that in dust grain environments, the ¹³CO₂ feature splits naturally at a certain temperature, independent of the surrounding ice layer, offering an alternative explanation for the observed double peak structure.

This work is based in part on observations made with the NASA/ESA/CSA James Webb Space Telescope. The data were obtained from the Mikulski Archive for Space Telescopes at the Space Telescope Science Institute, which is operated by the Association of Universities for Research in Astronomy, Inc., under NASA contract NAS 5-03127 for JWST. These observations are associated with program #1802. This work has been supported by the European Research Council under the Horizon 2020 Framework Program via the ERC Advanced Grant Origins 83 24 28. We would also like to acknowledge funding through the NanoSpace COST action (CA21126 - European Cooperation in Science and Technology) and Vector Stiftung (Project ID P2023-0152). The laboratory data generated for this study, along with select datasets presented in this paper, are available at: <https://doi.org/10.5281/zenodo.15728993>.

APPENDIX

During warming, the IR peak profile of the ν_3 band of ¹²CO₂ exhibited additional changes, summarized in Table 1. The most notable features include shifts in the LO mode and the appearance of shoulder peaks. These shoulders emerge in the spectral region between the LO and TO modes, with their positions and onset temperatures varying depending on the underlying surface.

T (K)	Au	Si	CO	CH ₄	pASW	CW	CH ₃ OH	CH ₃ OH:H ₂ O
30				shoulder at 2376				
35		shoulder at 2371					shoulders at 2376 and 2371	
40	shoulders at 2375 and 2368							
50				shoulder start to disappear				shoulder at 2376
55		shoulders shift to 2365				shoulder at 2364		
60	LO redshifts		LO red- shifts, shoulder at 2365	LO red- shifts, new shoul- ders at 2380 and 2371				
65	shoulders shift to 2380 and 2366				shoulder at 2376	shoulder disappear		
70		LO blueshifts						
75					shoulder disappear			
80							shoulders disappear	shoulder disappear

Table 1. Summary of IR spectral changes observed for the ν_3 band of $^{12}\text{CO}_2$ across different layered systems and temperatures.

REFERENCES

- Andersson, B. G., Lazarian, A., & Vaillancourt, J. E. 2015, ARA&A, 53, 501
- Baratta, G. A., Palumbo, M. E., & Strazzulla, G. 2000, A&A, 357, 1045
- Berremen, D. W. 1963, Phys. Rev., 130, 2193
- Boogert, A. C. A., Gerakines, P. A., & Whittet, D. C. B. 2015, ARA&A, 53, 541
- Boogert, A. C. A., Ehrenfreund, P., Gerakines, P. A., et al. 2000, A&A, 353, 349
- Bouilloud, M., Fray, N., Bénilan, Y., et al. 2015, MNRAS, 451, 2145
- Brunken, N. G. C., Rocha, W. R. M., van Dishoeck, E. F., et al. 2024, A&A, 685, A27
- Cooke, I. R., Fayolle, E. C., & Öberg, K. I. 2016, ApJ, 832, 5
- Edridge, J. L., Freimann, K., Burke, D. J., & Brown, W. A. 2013, Philos. Trans. R. Soc. A, 371, 20110578
- Ehrenfreund, P., Boogert, A. C. A., Gerakines, P. A., et al. 1996, A&A, 315, L341

- Ehrenfreund, P., Boogert, A. C. A., Gerakines, P. A., Tielens, A. G. G. M., & van Dishoeck, E. F. 1997, *A&A*, 328, 649
- Ehrenfreund, P., Kerkhof, O., Schutte, W. A., et al. 1999, *A&A*, 350, 240
- Emtiaz, S. M., Toriello, F., He, J., & Vidali, G. 2022, *JPCA*, 126, 1973
- Escribano, R. M., Munoz Caro, G. M., Cruz-Diaz, G. A., Rodríguez-Lazcano, Y., & Maté, B. 2013, *PNAS*, 110, 12899
- Falk, M., & Seto, P. F. 1986, *Can. J. Spectrosc.*, 31, 134
- Federman, S. A., Megeath, S. T., Rubinstein, A. E., et al. 2024, *ApJ*, 966, 41
- Fulker, J. E., McCoustra, M. R. S., & Brown, W. A. 2025, *ACS Earth Space Chem.*
- Fulvio, D., Sivaraman, B., Baratta, G. A., Palumbo, M. E., & Mason, N. J. 2009, *Spectrochim. Acta A*, 72, 1007
- Gerakines, P. A., Whittet, D. C. B., Ehrenfreund, P., et al. 1999, *ApJ*, 522, 357
- He, J., Acharyya, K., & Vidali, G. 2016, *ApJ*, 825, 89
- He, J., Emtiaz, S. M., & Vidali, G. 2017, *ApJ*, 837, 65
- He, J., Pérez Rickert, P. C., Suhasaria, T., et al. 2024, *Mol. Phys.*, 122, e2176181
- He, J., Toriello, F. E., Emtiaz, S. M., Henning, T., & Vidali, G. 2021, *ApJL*, 915, L23
- He, J., & Vidali, G. 2018, *MNRAS*, 473, 860
- Henning, T. 2010, *ARA&A*, 48, 21
- Ioppolo, S., Noble, J. A., Muiña, A. T., et al. 2022, *J. Mol. Spectrosc.*, 385, 111601
- Isokoski, K., Poteet, C. A., & Linnartz, H. 2013, *A&A*, 555, A85
- Jenniskens, P., & Blake, D. F. 1994, *Science*, 265, 753
- Lasne, J., Rosu-Finsen, A., Cassidy, A., McCoustra, M. R. S., & Field, D. 2015, *PCCP*, 17, 20971
- McClure, M. K., Rocha, W. R. M., Pontoppidan, K. M., et al. 2023, *NatAs*, 7, 431
- Minissale, M., Aikawa, Y., Bergin, E., et al. 2022, *ACS Earth and Space Chemistry*, 6, 597
- Öberg, K. I., Fayolle, E. C., Cuppen, H. M., van Dishoeck, E. F., & Linnartz, H. 2009, *A&A*, 505, 183
- Pontoppidan, K. M., Boogert, A. C. A., Fraser, H. J., et al. 2008, *ApJ*, 678, 1005
- Sabri, T., Gavilan, L., Jäger, C., et al. 2013, *ApJ*, 780, 180
- Sandford, S. A., & Allamandola, L. J. 1990, *ApJ*, 355, 357
- Suhasaria, T., Thrower, J. D., & Zacharias, H. 2017, *MNRAS*, 472, 389
- Tychengulova, A., Katpayeva, K., Shomshekova, S., et al. 2024, *ACS omega*, 10, 1237
- van Broekhuizen, F. A., Groot, I. M. N., Fraser, H. J., van Dishoeck, E. F., & Schlemmer, S. 2006, *A&A*, 451, 723